Cooling rate dependence of the properties for $Ti_{110}Al_{14}V_4$ alloy investigated by *ab initio* molecular dynamics

Jia Song [a], Luyu Wang [b], Ding Fan [a], Liang Zhang [a,*], Wenheng Wu [a], Zhibin Gao [c,*]

[a] *Shanghai Engineering Research Center of 3D Printing Materials, Shanghai, Research Institute of Materials, Shanghai 200437, China*
[b] *College of Artificial Intelligence and E-commerce, Hangzhou College of Commerce, Zhejiang Gongshang University, Hangzhou 311599, China*
[c] *State Key Laboratory for Mechanical Behavior of Materials, Xi'an Jiaotong University, Xi'an 710049, China*

ARTICLE INFO

ABSTRACT

The structural evolution and kinetic properties of $Ti_{110}Al_{14}V_4$ alloy under two constant cooling rates are comprehensively studied by *ab initio* molecular dynamics simulations. A variety of statistical methods are used to progressively analyze the changes in local atomic structure with temperature under different cooling rates. It is revealed that for slow cooling, the icosahedron and face-centered cubic (FCC) cluster dominate in the melt before the system transforms into a body-centered cubic (BCC) crystalline phase at a temperature of about 1600 K. For fast cooling, the system melts from 2600 to 1600 K, then turns into solid glass at 1400 K, and finally forms a crystalline and amorphous mixture. This is a process in which the icosahedron competes with the FCC structure, indicating that the $Ti_{110}Al_{14}V_4$ alloy has a very poor glass-forming ability because of the fragility of $Ti_{110}Al_{14}V_4$ liquids at high temperature. Furthermore, under a fast cooling rate, the self-diffusion coefficient obeys the Arrhenius function at high temperature but conforms to the mode coupling theory when approaching the critical temperature. Finally, through the five-fold local symmetry parameters and viscosity, a direct relationship between structure and dynamics is established, confirming that structural evolution is the root cause of slow dynamics. This discovery provides a new perspective on the structural mechanism of dynamic arrest in the $Ti_{110}Al_{14}V_4$ melt.

© 2021 Published by Elsevier B.V.

1. Introduction

Titanium and its alloys are widely used in modern industries and daily life because of their excellent corrosion resistance, biocompatibility, and high strength-to-weight ratio [1]. Among titanium alloys, Ti-6Al-4 V (TC4) is the most popular and is the preferred material for industrial applications of selective laser melting (SLM) manufactured products [2]. The SLM process involves melting and solidification of metal materials. It is well known that the macroscopic properties of metallic materials are essentially determined by their different microstructures, which in turn are largely influenced by the melt and cooling rates during solidification [3–6]. For a sufficiently fast cooling rate, an amorphous structure is formed through non-equilibrium thermodynamic processes, even for a monoatomic metal, while a slow cooling rate favors the formation of a crystalline structure [4]. Furthermore, the coexistence of crystalline and amorphous structures is favored under intermediate cooling rates, and the proportion and

distribution of the two structures depend on the cooling rate [6,7]. However, solidification is an extremely intricate physical phenomenon spanning a broad range of spatiotemporal scales, [8,9] and it is difficult to experimentally observe the nucleation and growth process for a supercooled melt *in situ* at the atomic level [10–12]. These reasons prevent us from thoroughly understanding the solidification process of TC4 melt.

Fortunately, these drawbacks have been conquered with the rapid development of computers. In 1953, Metropolis et al. introduced a computational simulation to study liquid metal, which pioneered the use of computers in the field of material design [13]. Since then, an increasing number of researchers have explored the microstructure of metallic melts by computational simulation, especially molecular dynamics technology. Xu et al. [14] used molecular dynamics with a new semi-empirical embedded atom potential to investigate the composition and temperature dependence of static and dynamic structures in Ni_xNb_{1-x} (x = 50–70 at.%). They found that the fraction of the perfect icosahedron was small in the liquid state but rose sharply during cooling and was dominant at 300 K. In addition, the self-diffusion coefficient and shear viscosity were insensitive to the Ni-Nb alloy composition. Ma et al. [15] employed *ab initio* molecular dynamics

(AIMD) to research the characteristics of a Ba-Bi liquid based on existing thermodynamic modeling. Their results showed that in the Ba-rich melt, the Bi-centered polyhedrons were strongly correlated to the crystalline structures of Ba_5Bi_3 and Ba_4Bi_3 with a longer lifetime than other polyhedrons during AIMD simulation, while in the Bi-rich melt, the Ba-centered polyhedrons were structurally diverse, short-lived, and poorly associated to $BaBi_3$ compound. Furthermore, molecular simulations have been used to study the cooling rate dependence of solidification for a liquid metal. Li et al. [5] used molecular dynamics simulations to study the effect of the cooling rate on the microstructure and mechanical properties of tungsten. The results showed that the increase of cooling rate reduced the degree of crystallization of tungsten, while the higher cooling rate inhibited the crack nucleation in cooling tungsten because of faster stress relaxation, which provided a promising method for the preparation of hybrid-structured tungsten with desirable mechanical properties. Hou et al. [4] studied the cooling rate dependence of solidification for liquid aluminum by a large-scale molecular dynamics simulation [4]. It was found that a fast cooling rate preferred amorphous structures with icosahedral features, while face-centered cubic (FCC) structures were formed by a slow cooling, at an intermediate rate, the coexistence of FCC and hexagonal close-packed (HCP) clusters was dominant. With the same method, Zhang et al. [3] researched the local structures of molten iron and their role in the nucleation process under various cooling rates. The simulation results revealed that the nucleation of iron was divided into three stages: first, there was a competition between icosahedral and crystalline clusters in supercooled melts; second, the transformation of the atomic configuration from icosahedron to crystal resulted in the growth and formation of medium-range order (MRO); third, the nucleation of body-centered cubic nuclei originated from the core of steady MRO clusters. In conclusion, molecular simulation is a useful tool to explore the details of the solidification process of metal melts.

From the above statements, it can be found that the cooling rate is an important factor affecting the local microstructure of metal melts during solidification. The local atomic clusters not only provide the necessary atoms for crystal nucleation but also determine the nucleation path. However, the local structure of TC4 alloys and their effect on nucleation remain unclear. Therefore, it is of great significance to study the evolution of the atomic clusters under different cooling conditions. For the first time, considering our computer resource, a $Ti_{110}Al_{14}V_4$ alloy with a mass fraction similar to that of TC4 alloy is designed to approximately shed light on the solidification mechanisms of molten TC4 alloy under two cooling rates by AIMD simulations. The simulated density of $Ti_{110}Al_{14}V_4$ alloy under two cooling rates is calculated first at different temperatures and compared with experimental values. Moreover, the variation of local atomic structure with temperature is statistically analyzed by the static structure factor and Voronoi tessellation. Finally, the dynamic properties of the $Ti_{110}Al_{14}V_4$ melt are discussed via self-diffusion coefficients and viscosity.

2. Methodology

AIMD simulations of the $Ti_{110}Al_{14}V_4$ alloy are implemented by the Vienna Ab-Initio Simulation Package (VASP) [16–20]. The exchange-correction energy of the electron is treated by the generalized gradient approximation (GGA) in the form of the Perdew-Burke-Ernzerhof (PBE) functional [21,22]. The electron–ion interaction is approximated by Projector-Augmented-Wave (PAW) pseudopotentials [23,24]. In this study, the maximum cutoff value for Ti, Al, and V are 222.3, 240.3, and, 263.7 eV, respectively, so the maximum cutoff value of this alloy is 263.7 eV. The energy cutoff is set to 500 eV for accurate simulation, which is 1.9 times the maximum

cutoff value of this alloy. The energy convergence criterion of the electronic self-consistency is set to 10^{-6} eV per atom [25]. Newton's equation of motion is solved through Verlet's algorithm with a time step of 3 fs. Spin polarization is used in the simulation because Ti, Al, and V contain unpaired electrons in their valence shells.

110 Ti, 14 Al, and 4 V atoms are randomly distributed in a cubic box with standard periodic boundary conditions, as shown in Fig. 1. The mass fractions of Ti, Al and V in this alloy are 90.0%, 6.46%, and 3.54%, which are similar to the TC4 alloy with approximately 90.0 wt% for Ti, 6.0 wt% for Al and 3.5–4.5 wt% for V, respectively [26,27]. Only the Γ point is considered to sample the Brillouin zone. The $Ti_{110}Al_{14}V_4$ configuration is heated to 2600 K, about 35.21% above the experimental value of 1923 K for the TC4 alloy, [27] to avoid the memory effect from the initial random structure. The molten alloy is then cooled stepwise down to 2400, 2200, 2000, 1800, 1600, 1400, 1200, 1000, and 800 K under two constant cooling rates of 1.33×10^{13} and 10^{15} K/s, denoted as v_1 and v_2, respectively. After quenching down to the desired temperature, the $Ti_{110}Al_{14}V_4$ supercells are subjected to molecular dynamics simulations in the NpT ensemble with a constant number, pressure, and temperature [28]. The temperature is controlled by the Langevin thermostat with a friction coefficient of 2 ps^{-1} for all atoms and 10 ps^{-1} for the lattice degrees of freedom. A mass of 5 amu is used for the lattice degrees of freedom. A total of 5000 steps (15 ps) for the NpT ensemble simulations are performed, and the final 2000 steps are selected to estimate the equilibrium volume. Eventually, the calculated equilibrium volume is used as an input configuration in the following 10,000 steps of the NVT ensemble simulations (constant number, volume, and temperature) with a Nosé-Hoover thermostat controlling temperature [29]. The first 8000 steps are used to relax the system to reach thermal equilibrium, and the remaining 2000 AIMD steps are used to analyze the structural and kinetic properties.

3. Results and discussions

3.1. The density of the $Ti_{110}Al_{14}V_4$ alloy

Fig. 2 shows the simulated densities evaluated from the NpT ensemble simulation and experimental densities derived from
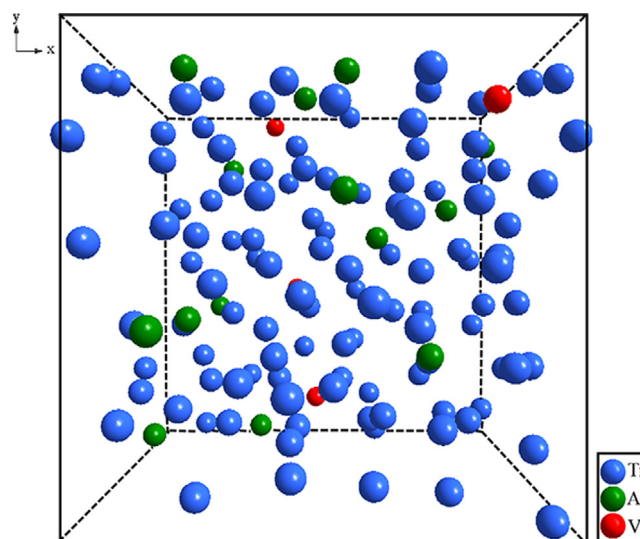

Fig. 1. Structural model of the $Ti_{110}Al_{14}V_4$ alloy, in which blue ball represents Ti atom, green ball represents Al atom, and red ball represents V atom. (For interpretation of the references to colour in this figure legend, the reader is referred to the web version of this article.)
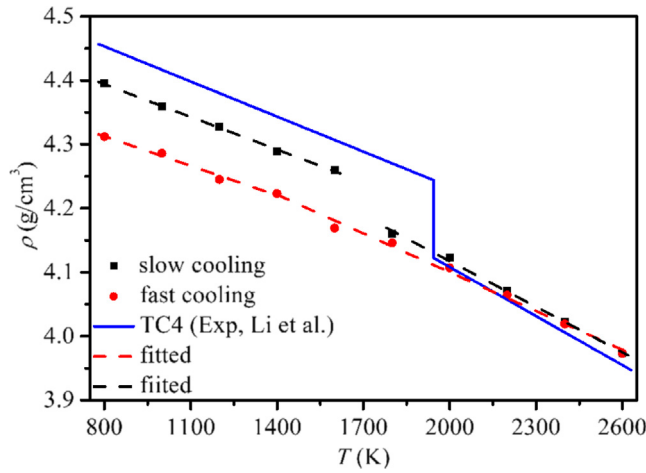
Fig. 2. AIMD density versus temperature during the cooling process of $Ti_{110}Al_{14}V_4$ under two constant rates compared with the experimental data of TC4 alloy measured by Li et al.[30]

previous reports [30]. Upon cooling from 2600 to 2000 K, the AIMD density varies between 3.973 and 4.123 g·cm^{-3} at v_1 and 3.973–4.107 g·cm^{-3} at v_2, respectively. The difference in density under the two cooling rates is exceedingly small, manifesting the weak effect of the cooling rate on the density at high temperature. Meanwhile, the corresponding experimental density of the TC4 alloy measured by Li et al. [30] increases from 3.955 g·cm^{-3} to 4.109 g·cm^{-3}. This indicates that our AIMD density of liquid $Ti_{110}Al_{14}V_4$ is genuinely like the experimental density with an absolute deviation between 0.04% and 0.45%, reflecting a good description of the interatomic interaction of liquid $Ti_{110}Al_{14}V_4$ by PBE functional. For low speeds, as the temperature drops further, an abrupt change is observed between 1800 and 1600 K. This phenomenon can be attributed to the crystallization of some atoms at this cooling rate. After that, the density increases continuously with decreasing temperature. In this case, the AIMD densities are divided into two segments for linear fitting within the scope of our research,

$$\rho = \begin{cases} 4.592 - 2.375 \times 10^{-4}T & (1800 \leqslant T \leqslant 2600) \\ 4.530 - 1.700 \times 10^{-4}T & (800 \leqslant T \leqslant 1600) \end{cases} \quad (1)$$

For high speed, the AIMD density increases step by step until the temperature drops to 1400 K, without the abrupt change observed in the experimental data at 1943 K or occurred from 1800 to 1600 K under the low cooling rate. Upon further lowering the temperature to 800 K, a distinct kink is detected around 1400 K, changing the slope to a small value of 1.540×10^{-4}. Overall, the temperature-dependent AIMD densities can also be fitted satisfactorily to a linear function over different temperature ranges,

$$\rho = \begin{cases} 4.500 - 2.006 \times 10^{-4}T & (1400 < T \leqslant 2600) \\ 4.436 - 1.540 \times 10^{-4}T & (800 \leqslant T \leqslant 1400) \end{cases} \quad (2)$$

Additionally, it is worth mentioning that in the low-temperature range, the AIMD density at a high cooling rate differs from the experimental value by approximately 0.132 g·cm^{-3}, which is larger than the difference between the AIMD density at a low cooling rate and the experimental value, about 0.055 g·cm^{-3}. [31] This is because under a high cooling rate, the rapid increase in the viscosity of the metal melt leads to some atoms to move so slowly that they do not have time to relax to equilibrium, which inhibits the crystallization process of atoms and forms the metal-glass structure.

3.2. Static structure factor

The static structure factor, $S(q)$, is an important physical quantity for describing the properties of liquid and overcooled liquid. The total static structure factor (TSSF) for $Ti_{110}Al_{14}V_4$ is defined as the weighted summation of all partials from the AIMD trajectory, [31]

$$S(q) = \sum_i \sum_j \frac{c_i c_j f_i f_j}{\left(\sum_i c_i f_i\right)^2} S_{ij}(q) \quad (3)$$

in which c_i (or c_j) is the composition of the components, f_i (or f_j) is the neutron scattering length of the corresponding particle, and $S_{ij}(q)$ is a partial static structure factor. The evolution of TSSF for $Ti_{110}Al_{14}V_4$ at two constant cooling rates over the temperature range of 2600 to 800 K is shown in Fig. 3. The variations in the main peaks under the two cooling rates are similar: with decreasing temperature, the shape becomes narrower, the peak value gradually shifts to a higher q, and the amplitude increases. The information means that the disorder degree of liquid $Ti_{110}Al_{14}V_4$ decreases and the order degree increases. The second peak of the two cooling rates is quite different when the temperature is below 1600 K. For slow cooling, the second peak decomposes into two separate peaks, which can be indexed to a body-centered cubic (BCC) structure. [32] For fast cooling, the second peak starts to split into two sub-peaks at 1400 K. The relationship between the positions of the sub-peaks and the main peaks can be used to characterize the different types of short-range order (SRO).[33] Table 1 lists the main position (q_{main}), first sub-peak (q_{fisrt}), second sub-peak (q_{second}) and the $q_{fisrt}(q_{second})/q_{main}$ ratio from 1400 to 1000 K. The main peak positions are located at 2.71–2.72 Å^{-1}, the first sub-peak positions are located at 4.64–4.70 Å^{-1}, and the second sub-peak positions are located at 5.19–5.22 Å^{-1}. The q_{first}/q_{main} and q_{second}/q_{main} ratios are calculated to be approximately 1.72 and 1.92, respectively, at various temperatures, corresponding to the icosahedral (ICOS) cluster. [33] Based on the peak shapes and ratios of different peak positions, it is concluded that the ICOS structure is formed by rapid cooling of the $Ti_{110}Al_{14}V_4$ melt, while the BCC structure is formed by slow cooling. Upon rapid cooling to 800 K, the TSSF pattern exhibits some changes. The value of the second sub-peak becomes larger than that of the first sub-peak. It is speculated that some new structures are formed. To determine the new structure and the percentage of each structure during the cooling process, Voronoi tessellation is discussed in the next section.

3.3. Voronoi tessellation analysis

Since the three-dimensional structure information provided by statistically average RDFs is limited, the Voronoi tessellation method is used to further explore the short-range arrangement of atoms. The Voronoi polyhedral is expressed by Schläfli's notation, $<n_3, n_4, n_5, n_6>$, where n_i is the number of faces with i vertices [34–36]. The Voronoi indices of perfect BCC, FCC, and ICOS are < 0, 6, 0, 8>, <0, 12, 0, 0>, and < 0, 0, 12, 0>, respectively.

It has been previously reported that the preference of a polyhedron depends on the effective atomic radius ratio between solute and solvent, R^*. With decreasing R^*, the preferred polyhedral changes from a Frank-kasper polyhedron ($R^* > 1.2$) to an icosahedron ($R^* < 0.902$), then to a bi-capped square Archimedean antiprism polyhedron ($R^* < 0.835$), and finally to a tricapped trigonal prism packing type polyhedron ($R^* < 0.732$). [37] In this study, R^* varies between 0.888 (V/Ti) and 1.021 (Al/Ti), predicting icosahedral dominance in the $Ti_{110}Al_{14}V_4$ melt. The top 16 populated Voronoi indices at various temperatures during different cooling processes are shown in Fig. 4. For fast cooling, in the melt state, the clusters prefer to form polyhedra with Voronoi indices of < 0,
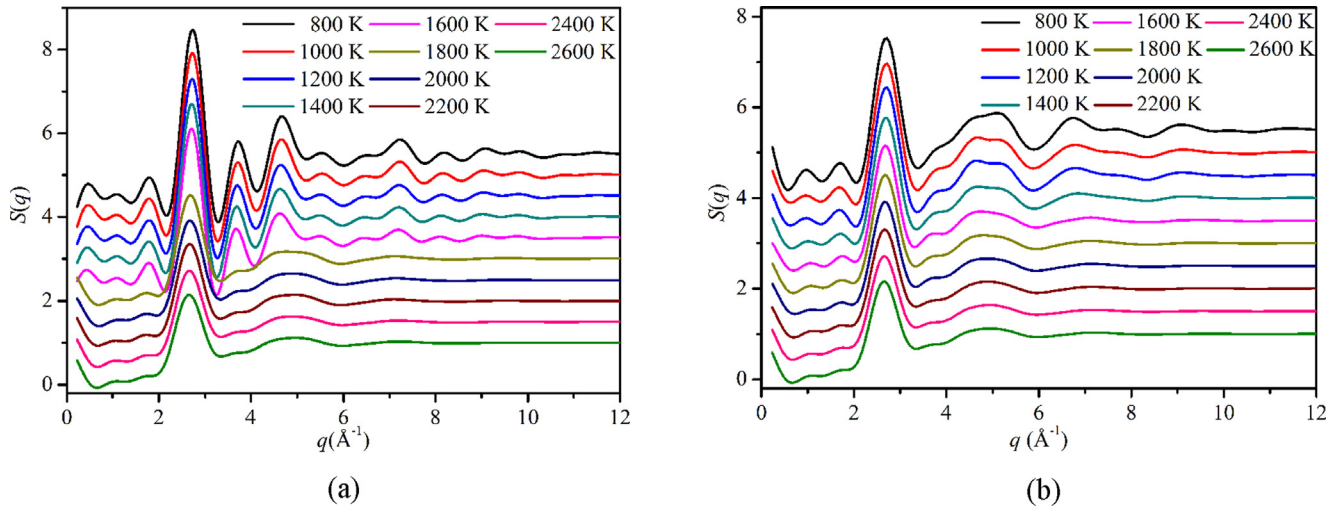
Fig. 3. Temperature dependence of the TSSF for $Ti_{110}Al_{14}V_4$ alloy under two cooling rates:(a) 1.33×10^{13} and (b) 10^{15} K/s. (Note that, for clarity, each curve has been vertically displaced from the curve below.)

Table 1
The main position q_{main}, first sub-peak q_{fisrt}, second sub-peak q_{second} and the $q_{fisrt}(q_{second})/q_{main}$ ratio from 1400 to 1000 K.

T (K)	q_{main} ($Å^{-1}$)	q_{fisrt} ($Å^{-1}$)	q_{second} ($Å^{-1}$)	q_{fisrt}/q_{main}	q_{second}/q_{main}
1000	2.72	4.70	5.19	1.73	1.91
1200	2.71	4.65	5.20	1.72	1.92
1400	2.71	4.64	5.22	1.71	1.93

0, 12, 0>, <0, 1, 12, 0>, <0, 2, 8, 2>, <0, 2, 8, 4>, <0, 3, 6, 3>, <0, 3, 6, 4>,<0, 3, 6, 5>, <0, 4, 4, 6>, <1, 3, 4, 5, 1>, and < 1, 3, 5, 4, 2>; in the solid glass, some new polyhedra are formed, <0, 6, 0, 8>, <0, 4, 4, 7>, <0, 5, 2, 6>, <0, 5, 2, 8>, <0, 1, 4, 3, 5, 2>, and < 0, 4, 4, 5 > . For slow cooling, in the melt state, the preferred polyhedron is basically consistent with fast cooling, whereas in solids, the polyhedra are < 0, 6, 0, 8>, <0, 4, 4, 6>, <0, 5, 2, 8>, <0, 5, 2, 6>, <0, 1, 5, 1, 5, 2>, <0, 1, 5, 1, 6, 2>, and < 0, 1, 4, 3, 5, 2 > .

To analyze the structural evolution of the $Ti_{110}Al_{14}V_4$ under different cooling rates in detail, these preferred polyhedra are classified into four categories according to Zhang et al. [3,32]: (a) < 0, 3, 6, 4>, <0, 3, 6, 5>, <0, 4, 4, 6>, and < 0, 4, 4, 7 > are considered to be FCC-like clusters; (b) < 0, 6, 0, 8 > represents BCC-like clusters; (c) < 0, 0, 12, 0>, <0, 1, 12, 0>, <0, 3, 6, 3>, and < 0, 2, 8, x> (x = 1, 2…4) represent ICOS-like clusters; (d) the remaining Voronoi indices are unknown structures. For slow cooling from 2600 to 1800 K, the percentage varies from 9.47% to 13.38% for the ICOS-like cluster and from 5.11% to 10.15% for the FCC-like cluster. At 1600 K, the percentage of ICOS-like clusters goes down dramatically to 0, while the percentage of BCC-like clusters, <0, 6, 0, 8>, rapidly rises to 37.19%. The percentage of some FCC-like clusters drops to 0, such as < 0, 3, 6, 4>, and < 0, 3, 6, 5>, and that of the other FCC-like cluster, <0, 4, 4, 6>, increases to 17.19%. In addition, some unknown structures appear, such as 8.26% <0, 5, 2, 8>, 7.73% <0, 5, 2, 6>, 4.68% <0, 1, 5, 1, 5, 2>, and 4.83% <0, 1, 5, 1, 6, 2 > . As the temperature further cools to 800 K, the percentage of BCC-like clusters goes up to 75.8%, the percentage of FCC-like clusters reduces to 6.14%, and the percentage of unknown structures drops to 4.25% for < 0, 5, 2, 8, 3.00% for < 0, 5, 2, 6>, 1.74% for < 0, 1, 5, 1, 5, 2>, and 1.60% for < 0, 1, 5, 1, 6, 2 > . The populations of < 0, 4, 4, 6>, <0, 5, 2, 8>, <0, 5, 2, 6>, <0, 1, 5, 1, 5, 2>, and < 0, 1, 5, 1, 6, 2 > increase at the beginning of crystallization but decrease as the degree of crystallization increases, revealing that these polyhedra play an important role in the crystallization process of the $Ti_{110}Al_{14}V_4$

melt.[3] Notably, a small portion of these clusters remain in the system at the end of crystallization and may serve as defects. For fast cooling, from 2600 to 1600 K, the percentage of ICOS-like and FCC-like clusters varies between 9.47 and 19.05% and 5.1–18.34%, respectively. ICOS-like and FCC-like clusters are prevalent in the $Ti_{110}Al_{14}V_4$ melt, and the percentage of ICOS-like clusters is higher than that for the FCC-like clusters at the beginning but gradually approaches the latter with decreasing temperature. In the temperature range of 1400–800 K, the percentage of ICOS-like clusters slightly decreases from 20.27% to 19.50%, while that of FCC-like clusters increases from 32.93% to 36.35%. BCC-like (<0, 6, 0, 8 >) and unknown clusters (<0, 5, 2, 8 > and < 0, 5, 2, 6 >) are formed, and their percentages vary from 1.79 to 7.73%, 3.03 to 6.09%, and 2.36 to 4.76%, respectively. It follows that the system is a mixture of crystalline and amorphous structures dominated by FCC-like and ICOS-like clusters in this temperature range.

In summary, for slow cooling, ICOS-like and FCC-like clusters dominate in the melt before the system transforms into a crystalline BCC phase at a temperature of approximately 1600 K. For fast cooling, the system melts from 2600 to 1600 K, turns into solid glass at 1400 K, and then finally forms a crystalline and amorphous mixture. The whole process is dominated by ICOS-like and FCC-like clusters. There are more ICOS-like clusters than FCC-like clusters in the melt, but the opposite is true in the mixture. The simulation snapshots from the melt at 2200 K to solid at 800 K under two cooling processes are displayed in Fig. 5.

Compared with the Cu-Zr-Al alloy,[39] even at a very high cooling rate of 10^{15} K/s, the $Ti_{110}Al_{14}V_4$ alloy still does not form amorphous structures but forms a mixture of amorphous and FCC-like clusters and gradually forms a BCC structure with a further decrease in temperature, which indicates that the alloy has a poor glass-forming ability (GFA). As previously reported, fragility is related to the GFA, where stronger liquids generally have a higher GFA than fragile liquids [40,41]. The strength of the liquid can be
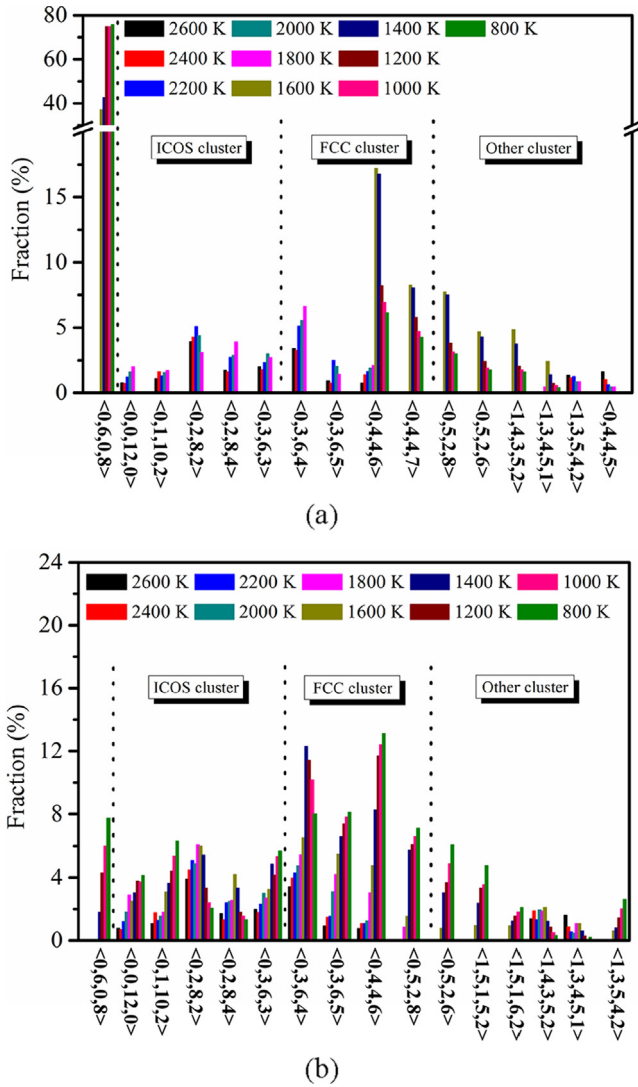
Fig. 4. The variation of main Voronoi indices in the Ti$_{110}$Al$_{14}$V$_4$ alloy with temperature under cooling rates of (a) 1.33×10^{13} and (b) 10^{15} K/s.
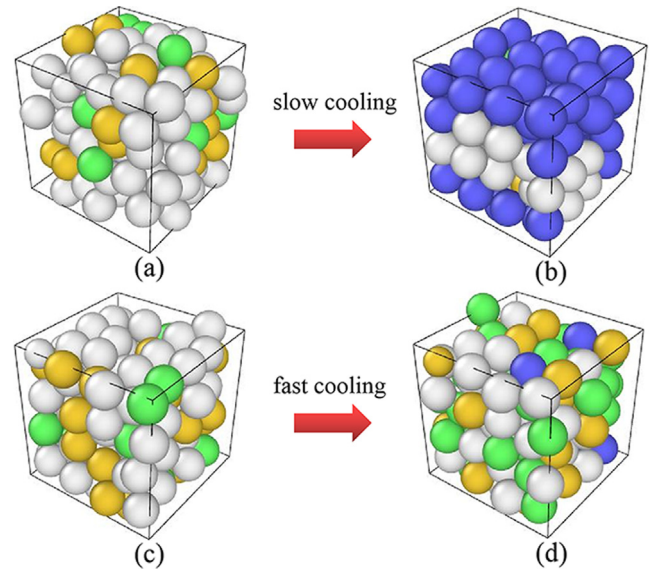

Fig. 5. Simulation snapshots of the melt (a and c) and solid (b and d) under two cooling rates: the upper layer is slow cooling, and the lower layer is fast cooling. The atoms in the snapshots are identified by common neighbor analysis with the standard visualization tool OVITO, [38] where the white balls represent atoms of other structures, the green balls represent FCC-like atoms, yellow balls represent ICOS-like atoms, and the blue balls represent BCC-like atoms. (For interpretation of the references to colour in this figure legend, the reader is referred to the web version of this article.)
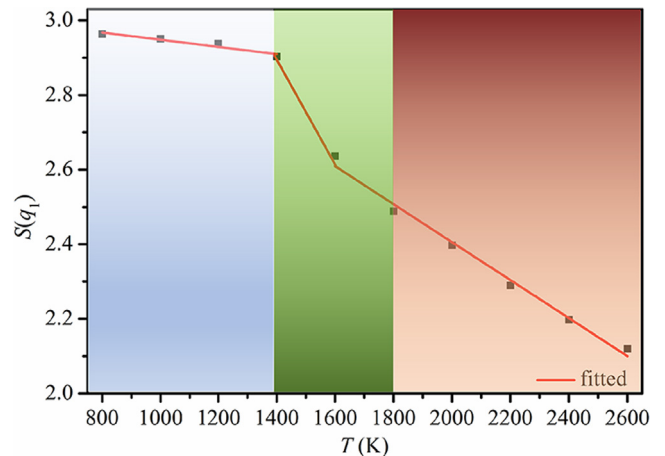

Fig. 6. The maximum value of the first peak in $S(q)$ as a function of temperature.

preliminarily determined by the structural index, $S(q)$. The height of the first peak in $S(q)$, marked as $S(q_1)$, changes with temperature under fast cooling, as shown in Fig. 6. Three distinct regions of behavior are observed for the growth of $S(q_1)$ with decreasing temperature: (1) at high temperature, the rate of change in $S(q_1)$, $dS(q_1)/dT$, is -5.09×10^{-4} K^{-1}; (2) below 1400 K, the $dS(q_1)/dT$ becomes -0.97×10^{-4} K^{-1}. The small rate of change is to be expected because there is no structural variation below 1400 K on laboratory timescales; (3) the intermediate region is an experimentally unreachable area linking the other two regions that require an acceleration in the development of $S(q_1)$. The $S(q_1)$ pattern of the Ti$_{110}$Al$_{14}$V$_4$ alloy under fast cooling is matched with that of fragile liquid. [40–42] Therefore, from the perspective of structural signature, it can be concluded that Ti$_{110}$Al$_{14}$V$_4$ alloy is a fragile liquid at high temperature and has a poor GFA.

3.4. Self-diffusion coefficients

Additional information about structure evolution can be obtained by investigating the atom movement during cooling. For example, the dynamic properties of Ti$_{110}$Al$_{14}$V$_4$ alloy are studied by calculating the mean-square displacement (MSD) as a function of time using the following equation,

$$\left\langle R_\alpha^2(t) \right\rangle = \frac{1}{N_\alpha} \left\langle \sum_{i=1}^{N\alpha} \left| R_{i\alpha}(t+\tau) - R_{i\alpha}(\tau) \right|^2 \right\rangle \quad (4)$$

where N_α is the total atomic number of α species, $R_{i\alpha}$ is the coordinates of atom i, and τ is the arbitrary origin of time. Fig. 7 displays the total MSD at the two cooling rates at different temperatures. Obviously, there are three regions: (i) For an extremely short period at first, all MSD traces increase in a quadratic form with relaxation time because of the ballistic motion of the atoms. At the same temperature, the slopes for the MSD are similar for both cooling rates, meaning that atoms move uniformly during this period; (ii) For the intermediate time period, at high temperature, intersections with the linear diffusion region are detected after ballistic growth, while at low temperature, due to the so-called "cage effect", plateaus appear in the MSD curves and become more prominent with decreasing temperature [43]. The caging
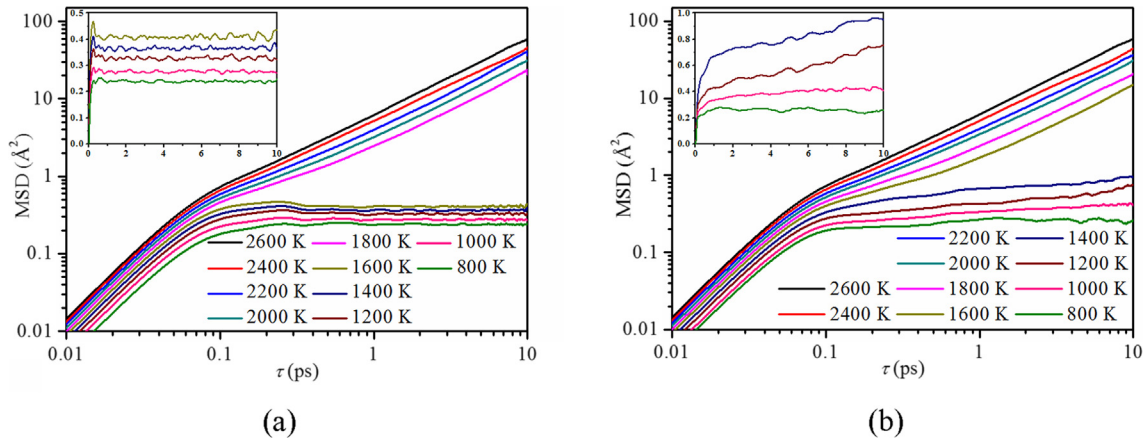
Fig. 7. MSD as a function of time under different cooling rates: (a) 1.33×10^{13} and (b) 10^{15} K/s.

effect is such that each atom is surrounded by an efficient cage formed by its neighbors, which limits the movement of the atom in a range close to its original position. From the Fig. 7, it is observed that during the intermediate time period, the MSD values remain at about 0.2 Å^2 after 1400 K for v_1 and 1600 K for v_2, indicating the occurrence of β-relaxation [44]. The different β-relaxation temperatures must be related to the structural heterogeneity; (iii) After a period of β relaxation, for a fast cooling rate, MSD trajectories present weak linear growth with time below 1400 K, as shown in the inset of Fig. 7b; that is, the atoms escape from the cage and diffuse for a short distance. For a low cooling rate, however, even after a sufficiently long time, when the temperature is lower than 1600 K, the MSD oscillates around an average, as illustrated in the inset of Fig. 7a, which means that the atoms cannot break free from the cage and are confined to the vicinity of the original position, with only thermal vibration. As temperature varies from 1600 to 800 K, the mean values are 0.36, 0.32, 0.25, and 0.23 Å^2. The oscillating MSD curves also confirm that Ti$_{110}$Al$_{14}$V$_4$ has already solidified at these temperatures.

Consequently, the total diffusion coefficients D are evaluated from the slope of the MSD curve based on the Einstein relation,

$$D_\alpha = \lim_{t \to \infty} \left\langle R_{i\alpha}^2(t) \right\rangle / 6t \tag{5}$$

Previously, some scholars have indicated that the MSD value should be greater than 4 Å^2 to obtain statistically significant diffusion information, otherwise, quantitative prediction of atomic self-diffusion coefficient is limited [45]. Therefore, we only calculate the total diffusion coefficients from 2600 to 1800 K for a slow cooling rate and from 2600 to 1600 K for a fast cooling rate in this study. The temperature dependence of the total self-diffusion coefficients under two cooling rates is shown in Fig. 8. It is obvious that in the temperature range of 2600–1800 K, the self-diffusion coefficients at the two cooling rates decrease with decreasing temperature and conform to the Arrhenius formula with an R^2 value of 0.99. The order of magnitude of the simulated data agrees with the assumption reported by Semiatin et al. [46] By fitting ln$D$ and 1/T to a linear function, as illustrated in the inset in Fig. 8, the activation energies of the alloy is obtained at 39.23 kJ/mol for v_1 and 43.63 kJ/mol for v_2, which is slightly less than the value of 52.8 kJ/mol reported by Iida [47]. The lower the activation energy, the faster the atoms move, which explains the higher self-diffusion coefficients at the lower cooling rate from the viewpoint of energy. Then, with a further decrease in temperature, the self-diffusion coefficients decrease faster than that predicted by the Arrhenius formula at the rapid cooling rate. This change means that the dynamics of homogeneous viscous flows at high
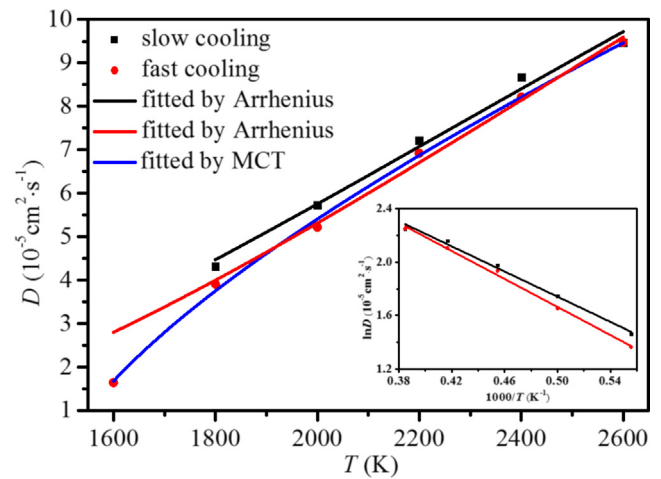

Fig. 8. Variation in the self-diffusion coefficients of the Ti$_{110}$Al$_{14}$V$_4$ melt with temperature under different cooling rates.

temperatures begin to become uneven. At this time, the self-diffusion coefficients of Ti$_{110}$Al$_{14}$V$_4$ melt can be fitted by the mode coupling theory (MCT) formula, [43,44] which is also known as the extended Arrhenius formula,

$$D = a(T - T_c)^r \tag{6}$$

where T_c is the critical temperature at which liquid relaxation bifurcation occurs and r is the critical exponent. As a result, T_c is fitted to be 1506.7 K, after which the liquid is no longer ergodic, and r is approximately equal to 0.70.

To further explore the relationship between the local atomic structure and dynamics, a five-fold symmetry parameter W is introduced and defined as, [41,48]

$$W = \sum_i \left(f_i^5 \times P_i \right) \tag{7}$$

where P_i represents the fraction of polyhedron type i, and f_i^5 is the fraction of the 5-edged polygon in the Voronoi polyhedron and obtained by the following formula,

$$f_i^5 = \frac{n_i^5}{\sum_{k=3,4,5,6} n_i^k} \tag{8}$$

in which n_i^k denotes the number of k-edged polygons in Voronoi polyhedron type i. The change of W with temperature in the Ti$_{110}$-Al$_{14}$V$_4$ alloy at two cooling rates is shown in Fig. 9. Visibly, from

2600 to 800 K, W of fast cooling increases with decreasing temperature, rapidly increases when the temperature approaches T_c and slightly increases after T_c, while W of slow cooling shows a tendency to gradually decrease with decreasing temperature after 1800 K and is almost 0 at 800 K. Beyond that, the fast cooling has more ICOS-like clusters and a larger W value compared with slow cooling, which is responsible for dynamical slowing during the fast cooling process for $Ti_{110}Al_{14}V_4$ alloy. This is because ICOS-like clusters often interpenetrate with each other, and these interpenetrating ICOS-like clusters have strong spatial correlation and produce stable string-like networks, thus reducing the melt dynamics [43,44].

3.5. Viscosity

To clarify the relationship between the kinetics and structure, the shear viscosity of the $Ti_{110}Al_{14}V_4$ melt, another key transport property describing the dynamics of liquid, is calculated by the Stokes-Einstein-Sutherland (SES) equation,

$$\eta = \frac{k_B T}{2\pi D_\alpha d_\alpha} \tag{9}$$

in which η is the shear viscosity of the alloy melt and d_α is the solvodynamic diameter. Apparently, the viscosity estimated via the SES equation is related to the self-diffusion coefficients and solvodynamic diameter, where the self-diffusion coefficients have been precisely calculated in Section 3.4, and the solvodynamic diameter is represented by the first peak position of radial distribution functions. At the fast cooling rate, the first peak position of radial distribution functions is between 2.81 and 2.83 Å over the temperature range of 2600–1600 K.

Fig. 10 shows the temperature dependence of the viscosity for the $Ti_{110}Al_{14}V_4$ melt above the critical temperature of 1506.7 K under a fast cooling rate. As the temperature is close to T_c, the viscosity increases sharply and does not follow the Arrhenius function, meaning dynamic deceleration during a fast cooling rate. The degree to which the viscosity reveals non-Arrhenius behavior is usually parameterized by fitting T and η to a Vogel-Fulcher-Tammann (VFT) formula, [41,48]

$$\eta = \eta_0 \exp(\frac{D^* T_0}{T - T_0}) \tag{10}$$

where η_0 is the viscosity at infinite liquidus temperature, T_0 is the temperature at which η becomes infinite, and D^* is a measurement index for the liquid fragility. D^* is a suitable parameter for assessing the fragility of liquids because the VFT formula follows
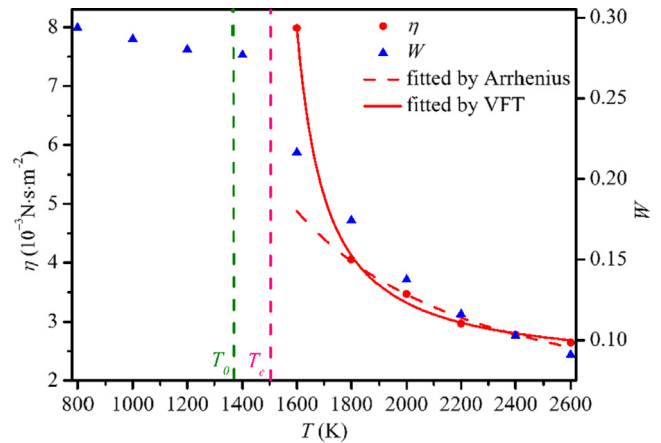

Fig. 10. The variation of η with temperature under two cooling rates above T_c and W versus temperature at a fast cooling rate. The fitted value of T_0 is 1388.8 K.

more Arrhenius-like behavior as D^* increases, consistent with stronger (less fragile) liquids. [48] In this study, the fitted value of D^* is 0.227, which is fairly small compared to other alloys, meaning that the $Ti_{110}Al_{14}V_4$ melt is a fragile liquid. As mentioned earlier, the more fragile the liquid, the weaker the GFA. Thus, we can draw a conclusion from a kinetic point of view that the $Ti_{110}-Al_{14}V_4$ alloy has a weak GFA. In addition, the five-fold symmetry parameters (W) at a fast cooling rate are displayed for further exploration. As shown in Fig. 10, the changing trends of W and η with temperature are similar above T_c. Therefore, it is speculated that the change of viscosity may be related to the evolution of the basic structure [41,48,49].

To build a quantitative relation between η and W, the power law $(1-W) \sim (T-T_1)^\alpha$ is used to fit W as a function of temperature, as shown in the inset of Fig. 11. [50] The fitted value of T_1 is 1387.5 K, which is almost the same as that of T_0 at 1388.8 K. T_1 and T_0 are approximately equal to 0.92 times T_c. Therefore, by replacing T_0 in the VFT formula with T_1, the temperature can be eliminated, and a direct relationship between W and η can be obtained,

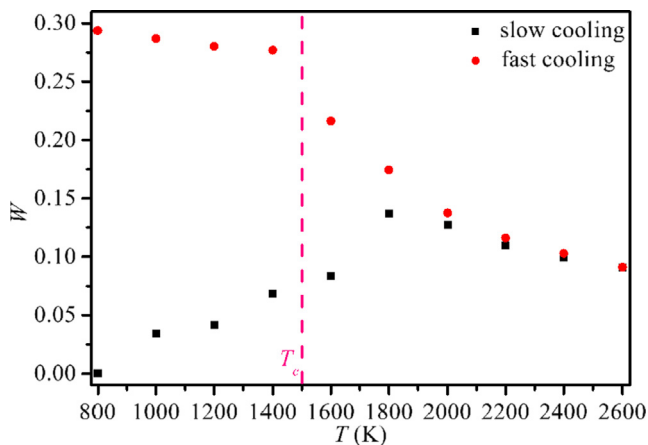$$\eta = \eta_0 \exp\left(\frac{B}{(1-W)^\delta}\right) \tag{11}$$

Fig. 9. Temperature dependence of W for the $Ti_{110}Al_{14}V_4$ alloy at two cooling rates.
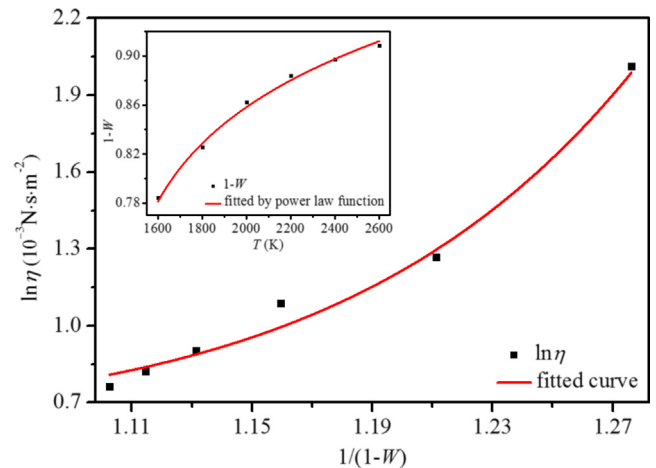

Fig. 11. The viscosity η as a function of W. The inset shows the temperature dependence of W.

where δ reflects the sensitivity of viscosity changes to local structural changes. As shown in Fig. 11, the simulated data are fitted well by Equation (11), and the statistical correlation parameter R^2 is 0.98. The fitted value for δ is 13.43, which is much larger than 1, indicating that small changes in structure can lead to significant changes in viscosity. In conclusion, structural evolution is the fundamental driver for dynamic deceleration, and the "hidden" structural changes resulting in the extremely dynamic variation of supercooled liquids can be distinctly described by the structural parameter W.

4. Conclusions

In this work, AIMD simulations are used to investigate the structural evolution and transport characteristics of the $Ti_{110}Al_{14}V_4$ alloy under two constant cooling rates. The density is first calculated from AIMD simulations in the NpT ensemble, which changes with temperature. At high temperatures, the AIMD density is almost unaffected by the cooling rate and is close to the experimental value. As the temperature decreases, there is a sudden change in the AIMD density between 1600 and 1800 K under a slow cooling rate but only a kink at 1400 K under a fast cooling rate.

After that, the trajectory of the system generated by the AIMD simulations is analyzed by static structure factor and Voronoi tessellation. These analytical methods reveal step by step the structural evolution of $Ti_{110}Al_{14}V_4$ alloy at different cooling rates. For slow cooling, the ICOS-like and FCC-like clusters dominate in the melt before the system transforms into a crystalline BCC phase at a temperature of about 1600 K. For fast cooling, the system is a melt from 2600 to 1600 K, turns into solid glass at 1400 K, and finally forms a mixture of crystalline and amorphous structures. The whole process is dominated by ICOS-like and FCC-like clusters. There are more ICOS-like clusters than FCC-like clusters in the melt, but the opposite is true in the mixture. In summary, even at a very high cooling rate of 10^{15} K/s, the $Ti_{110}Al_{14}V_4$ alloy still does not form amorphous structures but forms a mixture of amorphous and FCC-like clusters because at high temperatures, the $Ti_{110}Al_{14}V_4$ melt is a fragile liquid with a poor GFA.

From the perspective of kinetic properties, there are three conclusions. First, due to the more ICOS-like clusters in the melt, the self-diffusion coefficient of fast cooling is less than that of slow cooling. Moreover, under a fast cooling rate, the self-diffusion coefficient obeys the Arrhenius function at high temperature but conforms to the MCT when approaching the critical temperature. Eventually, a simple and straightforward relation between structure and dynamics is established by five-fold local symmetry parameter W and viscosity η, confirming that structural evolution is the underlying reason for the dynamic slowdown. Our findings provide a new perspective on the structural mechanism for dynamic arrest in $Ti_{110}Al_{14}V_4$ melt.

CRediT authorship contribution statement

Jia Song: Conceptualization, Investigation, Methodology, Validation, Data curation, Formal analysis, Visualization, Software, Writing – original draft, Writing – review & editing. **Luyu Wang:** Validation, Investigation. **Ding Fan:** Funding acquisition, Writing – review & editing. **Liang Zhang:** Funding acquisition, Resources, Supervision. **Wenheng Wu:** Resources, Supervision. **Zhibin Gao:** Funding acquisition, Resources, Supervision.

Declaration of Competing Interest

The authors declare that they have no known competing financial interests or personal relationships that could have appeared to influence the work reported in this paper.

References

[1] J.J. Yang, H.C. Yu, J. Yin, et al., Formation and control of martensite in Ti-6Al-4V alloy produced by selective laser melting, Mater. Design 108 (2016) 308–318.
[2] S.Y. Liu, Y.C. Shin, Additive manufacturing of Ti6Al4V alloy: a review, Mater. Des. 164 (2019) 107552.
[3] Q. Zhang, J.C. Wang, S. Tang, et al., Molecular dynamics investigation of the local structure in iron melts and its role in crystal nucleation during rapid solidification, Phys. Chem. Chem. Phys. 21 (2019) 4099–4674.
[4] Z.Y. Hou, K.J. Dong, Z.A. Tian, et al., Cooling rate dependence of solidification for liquid aluminium: a large-scale molecular dynamics simulation study, Phys. Chem. Chem. Phys. 18 (2016) 17461–17469.
[5] S.X. Li, S.Y. Cui, H.T. Chen, et al., Effect of cooling rates on solidification, microstructure and mechanical properties in tungsten, CrystEngComm 21 (2019) 3930–3938.
[6] C.S. Liu, J. Xia, Z.G. Zhu, et al., The cooling rate dependence of crystallization for liquid copper: A molecular dynamics study, J. Chem. Phys. 114 (2001) 7506–7512.
[7] Z.A. Tian, R.S. Liu, H.R. Liu, et al., Molecular dynamics simulation for cooling rate dependence of solidification microstructures of silver, J. Non-Cryst. Solids 354 (2008) 3705–3712.
[8] Y. Shibuta, S. Sakane, T. Takaki, M. Ohno, Submicrometer-scale molecular dynamics simulation of nucleation and solidification from undercooled melt: link age between empirical interpretation and atomistic nature, Acta Mater. 105 (2016) 328–337.
[9] S. Okita, E. Miyoshi, S. Sakane, et al., Grain growth kinetics in submicrometer-scale molecular dynamics simulation, Acta Mater. 153 (2018) 108–116.
[10] E. Liotti, A. Lui, R. Vincent, et al., A synchrotron X-ray radiography study of dendrite fragmentation induced by a pulsed electromagnetic field in an Al-15Cu alloy, Acta Mater. 70 (2014) 228–239.
[11] C. Ma, L. Chen, C. Cao, X. Li, Nanoparticle-induced unusual melting and solidification behaviours of metals, Nat. Commun. 8 (2017) 14178.
[12] L. Zhong, J. Wang, H. Sheng, et al., Formation of monatomic metallic glasses through ultrafast liquid quenching, Nature 512 (2014) 177.
[13] N. Metropolis, A.W. Rosenbluth, M.N. Rosenbluth, A.H. Teller, E. Teller, Equation of state calculations by fast computing machines, J. Chem. Phys. 21 (6) (1953) 1087–1092.
[14] T.D. Xu, X.D. Wang, H. Zhang, et al., Structural evolution and atomic dynamics in Ni-Nb metallic glasses: A molecular dynamics study, J. Chem. Phys. 147 (2017) 144503.
[15] J. Ma, S.-L. Shang, H. Kim, Z.-K. Liu, An ab initio molecular dynamics exploration of associates in Ba-Bi liquid with strong ordering trends, Acta Mater. 190 (2020) 81–92.
[16] Y.u. Zhang, J. Song, X. Li, L. Yan, S. Shi, T. Jiang, S. Peng, First principles calculation of redox potential for tetravalent actinides in molten LiCl-KCl eutectic based on vertical substitution and relaxation, Electrochim. Acta 293 (2019) 466–475.
[17] X.L. Wang, Q. Yu, X.D. Wang, et al., Tempeature-induced structural changes in the liquid GaInSn eutectic alloy, J. Phys. Chem. C 125 (2021) 7413–7420.
[18] Y.u. Su, X. Wang, Q. Cao, D. Zhang, J.-Z. Jiang, Different thermal responses of local structures in Pd43Cu27Ni10P20 alloy from glass to liquid, J. Phys. Chem. C 124 (36) (2020) 19817–19828.
[19] G. Kresse, J. Hafner, Ab initio molecular dynamics for liquid metals, Phys. Rev. B 47 (1993) 558.
[20] G. Kresse, J. Furthmüller, Efficient iterative schemes for ab initio total-energy calculations using a plane-wave basis set, Phys. Rev. B 54 (1996) 11169.
[21] J.P. Perdew, K. Burke, M. Ernzerhof, Generalized gradient approximation made simple, Phys. Rev. Lett. 77 (1996) 3865.
[22] J.P. Perdew, K. Burke, Comparison shopping for a gradient-corrected density functional, Int. J. Quant. Chem. 57 (3) (1996) 309–319.
[23] P.E. Blöchl, Projector augmented-wave method, Phys. Rev. B 50 (24) (1994) 17953–17979.
[24] G. Kresse, D. Joubert, From ultrasoft pseudopotentials to the projector augmentedwave method, Phys. Rev. B 59 (1999) 1758.
[25] J. Song, L.Y. Wang, L. Zhang, et al., First-principles molecular dynamics studying the solidification of Ti-6Al-4V alloy, J. Mol. Liq. 315 (2020) 113606.
[26] N. Milošević, I. Aleksić, Thermophysical properties of solid phase Ti-6Al-4V alloy over a wide temperature range, Int. J. Mater. Res. 103 (2012) 707–714.
[27] M. Boivineau, C. Cagran, D. Doytier, V. Eyraud, M.-H. Nadal, B. Wilthan, G. Pottlacher, Thermophysical properties of solid and liquid Ti-6Al-4V (TA6V) alloy, Int. J. Thermophys. 27 (2) (2006) 507–529.

[28] S. Melchionna, G. Ciccotti, B. Lee Holian, Hoover NPT dynamics for systems varying in shape and size, Mol. Phys. 78 (3) (1993) 533–544.

[29] C.Q. Xu, M.S. Lee, Y.G. Wang, et al., Structural Rearrangement of Au-Pd Nanoparticles under Reaction Conditions: An *ab Initio* Molecular Dynamics Study, ACS Nano 11 (2017) 1649–1658.

[30] J.J.Z. Li, W.L. Johnson, W.K. Rhim, Thermal expansion of liquid Ti-6Al-4V measured by electrostatic levitation, Appl. Phys. Lett. 89 (2006) 111913.

[31] T. Egami, S.J.L. Billinge, Underneath the Bragg peaks: Structural analysis of complex materials, in: R.W. Cahn (Ed.), Pergamon materials series, vol. 7, Elsevier, Oxford, 2003.

[32] Y.Q. Cheng, E. Ma, Atomic-level structure and structure-property relationship in metallic glasses, Prog. Mater. Sci. 56 (4) (2011) 379–473.

[33] G.W. Lee, A.K. Gangopadhyay, R.W. Hyers, et al., Local structure of equilibrium and supercooled Ti-Zr-Ni liquids, Phys. Rev. B 77 (2008) 184102.

[34] Y.D. Wei, P. Peng, Z.Z. Yan, et al., A comparative study on local atomic configurations characterized by cluster-type-index method and Voronoi polyhedron method, Comput. Mater. Sci. 123 (2016) 214–223.

[35] A. Hirata, L.J. Kang, T. Fujita, et al., Geometric frustration of icosahedron in metallic glasses, Science 341 (2013) 376–379.

[36] Q. Yu, X.D. Wang, H.B. Lou, Q.P. Cao, J.Z. Jiang, Atomic packing in Fe-based metallic glasses, Acta Mater. 102 (2016) 116–124.

[37] H.W. Sheng, W.K. Luo, F.M. Alamgir, J.M. Bai, E. Ma, Atomic packing and short-tomedium-range order in metallic glasses, Nature 439 (7075) (2006) 419–425.

[38] A. Stukowski, Visualization and analysis of atomistic simulation data with OVITO-the Open Visualization Tool, Modelling Simul. Mater. Sci. Eng. 18 (2010) 015012.

[39] M. Celtek, S. Sengul, U. Domekeli, Glass formation and structural properties of $Zr_{50}Cu_{50-x}Al_x$ bulk metallic glasses investigated by molecular dynamics simulations, Intermetallics 84 (2017) 62–73.

[40] N.A. Mauro, A.J. Vogt, M.L. Johnson, J.C. Bendert, K.F. Kelton, Anomalous structural evolution in $Cu_{50}Zr_{50}$ glass-forming liquids, Appl. phys. Lett. 103 (2) (2013) 021904, https://doi.org/10.1063/1.4813389.

[41] N.A. Mauro, M. Blodgett, M.L. Johnson, et al., A structural signature of liquid fragility, Nat. Commun. 5 (2014) 4616.

[42] K.F. Kelton, Kinetic and structural fragility-a correlation between structures and dynamics in metallic liquids and glasses, J. Phys.: Condens. Matter. 29 (2017) 023002.

[43] Y. Cheng, Y.Y. Wang, C.X. Peng, Z.T. Zhang, P.F. Wang, L.J. Jia, X.L. Li, L. Wang, Dynamic and structural heterogeneity in undercooled miscible and immiscible metallic liquid, J. Alloy Compd. 786 (2019) 627–635.

[44] S.K. Das, J. Horbach, T. Voigtmann, Structural relaxation in a binary metallic melt: molecular dynamics computer simulation of undercooled $Al_{80}Ni_{20}$, Phys. Rev. B 78 (2008) 064208.

[45] J.J. Han, W.Y. Wang, X.J. Liu, et al., Effect of solute atoms on glass-forming ability for Fe-Y-B alloy: an *ab initio* molecular dynamics study, Acta Mater. 77 (2014) 96–110.

[46] S.L. Semiatin, V.G. Ivanchenko, O.M. Ivasishin, Diffusion models for evaporation losses during electron-beam melting of alpha/beta-titanium alloys, Metall. Mater. Trans. B Process Metall. Mater. Process. Sci. 35 (2) (2004) 235–245.

[47] T. Iida, R. Guthrie, N. Tripathi, A model for accurate predictions of self-diffusivities in liquid metals, semimetals, and semiconductors, Metall. Mater. Trans. B Process Metall. Mater. Process. Sci. 37 (4) (2006) 559–564.

[48] Y.C. Hu, F.X. Li, M.Z. Li, et al., Five-fold symmetry as indicator of dynamic arrest in metallic glass-forming liquids, Nat. Commun. 6 (2015) 8310.

[49] C.A. Angell, Formation of glasses from liquids and biopolymers, Science 267 (5206) (1995) 1924–1935.

[50] F.W. Starr, S. Sastry, J.F. Douglas, What do we learn from the local geometry of glass-forming liquids?, Phys Rev. Lett. 89 (2002) 125501.